A functional error analysis of differential optical flow methods

Keishi Kumashiro · Adam M. Steinberg · Masayuki Yano

Abstract We analyze the sources of error in differential optical flow methods using techniques for the analysis of partial differential equations. We first derive an *a priori* error bound for the estimated optical flow field. We then systematically interpret this error bound and show that the estimation error is primarily bounded by the *best-fit approximation error* — which quantifies the fidelity with which one can represent the true optical flow field by a chosen or learned set of basis functions — divided by a *stability constant* — which quantifies one's ability to infer the optical flow field given the information content of the acquired data. We also show that the estimation error is bounded by effects associated with the finite temporal and spatial resolution of the acquired data. In particular, we show that the main finite resolution effects are related to the finite differencing and time-averaging of the measured intensity fields. Finally, we demonstrate the error bound numerically using synthetic three-dimensional data sets based on direct numerical simulations of homogeneous isotropic turbulence and transitional boundary layer flow provided by Johns Hopkins University (Li Y. et al. (2008) J. Turbulence 9:31, Zaki T.A. (2013) Flow Turbul. Combust.).

Keishi Kumashiro · Masayuki Yano
Institute for Aerospace Studies,
University of Toronto, Toronto ON, M3H 5T6, Canada
keishi.kumashiro@mail.utoronto.ca
myano@utias.utoronto.ca

Adam M. Steinberg
Daniel Guggenheim School of Aerospace Engineering,
Georgia Institute of Technology, Atlanta, GA 30332, USA
adam.steinberg@gatech.edu

1 Introduction

Optical flow (OF) is a concept introduced by the psychologist Gibson (1950) that is qualitatively defined as the apparent motion of brightness patterns within an image plane. OF motion estimation (OFME) is a computer vision framework dating back to the early 1980s (Horn and Schunck, 1981; Lucas and Kanade, 1981; Lucas, 1984) that systematically quantifies this notion. Tersely stated, the goal of OFME is to determine the *OF field* in a region of interest. Historically, OFME has been used most extensively for rigid and quasi-rigid body motion estimation (Horn and Schunck, 1981; Lucas and Kanade, 1981; Lucas, 1984; Enkelmann, 1988; Bergen et al, 1992; Barron et al, 1994; Beauchemin and Barron, 1995; Mémin and Pérez, 1998; Cohen and Herlin, 1999; Wu et al, 2000; Fleet and Weiss, 2005). Despite this origin, OFME has also found increasing adoption in fluid velocimetry (Corpetti et al, 2002; Heitz et al, 2009; Zhong et al, 2017; Ruhnau et al, 2004; Ruhnau and Schnörr, 2007; Schmidt and Sutton, 2019, 2020; Ruhnau et al, 2007; Corpetti et al, 2006; Yuan et al, 2007; Heitz et al, 2008; Quénot et al, 1998).

The interest in OFME methods for fluid velocimetry is due to their potential as alternatives or supplements to particle image velocimetry (PIV). A motion estimation framework based on the cross-correlation of successive particle image pairs, PIV is capable of providing robust velocity field estimates of particle-laden flows with low to medium seeding densities (Raffel et al, 2018; Elsinga et al, 2006; Scarano, 2012). However, PIV has constitutional limitations in terms of both spatial resolution and accuracy (Raffel et al, 2018), the latter being especially compromised when velocity gradients within PIV interrogation regions (IR) are significant. In contrast, OFME is non-correlational and, hence, lim-

ited in spatial resolution and accuracy solely by the information contained within the acquired data.

However, compared to PIV, the underlying sources of uncertainty in OFME fluid velocimetry are less understood. Indeed, results from OFME fluid velocimetry often are presented with vectors at every pixel in the domain — even though this greatly exceeds the information present in the underlying data — and without uncertainty quantification (UQ). This paper presents a rigorous *a priori* error analysis of the OFME fluid velocimetry estimation problem using error analysis techniques for the approximation of partial differential equations (PDEs), yielding an error bound that articulates the influence of various physical and numerical factors on the ultimate velocity uncertainty.

Fundamentally, OFME methods estimate the OF field by invoking some condition of photometric invariance (Barron et al, 1994; Fleet and Weiss, 2005; Corpetti et al, 2002; Heitz et al, 2009; Zhong et al, 2017). Within the context of rigid and quasi-rigid body motion estimation, OFME methods are almost invariably predicated on the *brightness constancy constraint* (Barron et al, 1994; Beauchemin and Barron, 1995; Weickert and Schnörr, 2001a), which is the condition in which the registered image intensity is neither generated nor destroyed in the measurement region. Instead, it is simply *transported* according to the underlying motion of objects within the region.

Provided that the image intensity field is sufficiently smooth, we may formalize the brightness constancy constraint as (Horn and Schunck, 1981)

$$\partial_t I(\underline{x}, t) + \underline{\nabla} I(\underline{x}, t) \cdot \underline{u}(\underline{x}, t) = 0 \quad \forall \underline{x} \in \Omega, \ \forall t \in T, \quad (1)$$

where $\Omega \subset \mathbb{R}^{n_d}$ is the measurement region; $T := [t_0, t_0 + \Delta t]$ is the measurement time domain; $I : \Omega \times T \to \mathbb{R}$ is the image intensity field; $\underline{u} : \Omega \times T \to \mathbb{R}^{n_d}$ is the OF field; and n_d is the number of spatial dimensions under consideration. Equation (1) is a differential statement of the transport of the (approximately) known image intensity I due to the unknown OF field $\underline{u}$. It is one of the prototypical constraint equations of OFME and is known as the *gradient constraint equation* (GCE) (Barron et al, 1994) or the OF constraint equation (Heitz et al, 2009; Weickert and Schnörr, 2001a). Indeed, a myriad of OF techniques are based on the GCE, or variations thereof (Barron et al, 1994; Corpetti et al, 2002; Heitz et al, 2009; Ruhnau et al, 2004; Ruhnau and Schnörr, 2007; Schmidt and Sutton, 2019, 2020). In the literature, such techniques are broadly classified as *differential methods* (Barron et al, 1994; Heitz et al, 2009; Weickert and Schnörr, 2001a).

Strictly speaking, OF is a two-dimensional (2D) concept. Therefore, OFME is technically a 2D framework.

However, we may also envision a setting in which (1) is applied to a three-dimensional (3D) intensity field, such as one inferred by tomographic reconstruction. In this paper, we treat both 2D and 3D cases. As such, we allow the number of dimensions n_d under consideration to equal either two or three, albeit at the expense of an abuse of terminology.

While the design of an OFME method requires a choice of which photometric invariance condition to invoke, it is also true that a single photometric invariance condition cannot fully constrain the OFME problem. For example, the GCE only constrains the component of $\underline{u}$ that is normal to the level sets of I (Horn and Schunck, 1981; Lucas and Kanade, 1981; Bergen et al, 1992; Barron et al, 1994; Beauchemin and Barron, 1995; Heitz et al, 2009). In order to resolve this closure problem — known in the literature as the *aperture problem* (Barron et al, 1994; Heitz et al, 2009) — additional prior information must be invoked.

With respect to differential methods, these additional prior constraints are generally divided into two categories: (i) localized or region-based schemes and (ii) global variational schemes (Barron et al, 1994; Heitz et al, 2009). The prototype of the former category is the Lucas-Kanade (1981; 1984) method, which stipulates that the OF field $\underline{u}$ is comprised of patches, within each of which the value of $\underline{u}$ is constant. Once Ω is partitioned into a prescribed grid of patches, the value of $\underline{u}$ in a given patch can then be computed by a weighted linear least squares fit of the GCE over the patch (Lucas and Kanade, 1981; Lucas, 1984; Barron et al, 1994; Beauchemin and Barron, 1995). The presumption of a piecewise constant $\underline{u}$ is particularly well-suited to rigid and quasi-rigid body motion estimation. As a result, the Lucas-Kanade method and its derivatives are widely used in computer vision (Barron et al, 1994; Beauchemin and Barron, 1995).

On the other hand, the prototypical global variational scheme is the Horn-Schunck (1981) method, which stipulates that $\underline{u}$ is the minimizer of a cost function J defined by

$$J(\underline{w}) := \int_{\Omega} \left((\partial_t I + \underline{\nabla} I \cdot \underline{w})^2 + \lambda_r \sum_{i=1}^{n_d} \|\underline{\nabla} w_i\|_2^2 \right) d\underline{x}, \quad (2)$$

where λ_r is a *regularization constant*. The cost function J consists of (i) a *data term*, which in this case quantifies the consistency of the photometric information and the OF field estimate $\underline{w}$ with the GCE, and (ii) a first-order *regularization term*, which imposes a global smoothness condition on $\underline{u}$. The regularization parameter λ_r simply sets the effect of the regularization term relative to the data term. In general, global variational

methods are predicated on cost functions of the same or similar form as (2) (Heitz et al, 2009).

As Heitz et al (2009) indicate in their review paper, most OFME methods developed and used for fluid velocimetry can be classified as variational. A notable exception is the first documented study of OFME fluid velocimetry (Quénot et al, 1998), which presents and demonstrates a method based on image matching and dynamic programming. Heitz et al (2009) assert that variational methods are favored in fluid velocimetry because they are amenable to supplementation by additional structural or physical constraints.

Indeed, much of the research in this area has been devoted towards the refinement of variational OFME methods in order to achieve improvements in the accuracy and spatial resolution of fluid flow estimates (Heitz et al, 2009). Moreover, most of this refinement occurs in variations of either the data term (Béréziat et al, 2000; Haußecker and Fleet, 2001; Brox et al, 2004; Papenberg et al, 2006; Brox and Malik, 2010), regularization term (Weickert and Schnörr, 2001a; Ruhnau and Schnörr, 2007; Ruhnau et al, 2007; Suter, 1994) or both (Corpetti et al, 2002; Zhong et al, 2017; Corpetti et al, 2006; Yuan et al, 2007). For instance, Corpetti et al (2002, 2006) propose a method that features (i) the Suter (1994) regularizer, which enforces smoothness of the divergence and curl of the OF field, and (ii) a physics-based variant of the GCE that they call the *integrated continuity equation* (ICE). Combining the more conservative second-order Suter regularizer with the physics-based ICE, Corpetti et al (2002, 2006) demonstrate a method that is particularly well suited to meteorological fluid velocimetry (Heitz et al, 2009; Cuzol et al, 2007; Héas et al, 2007). Other notable examples of variational OFME methods include those that incorporate physical constraints explicitly. These include methods that directly incorporate governing equations, such as mass conservation for constant density flows (Ruhnau and Schnörr, 2007; Álvarez et al, 2009) or the Stokes equations (Ruhnau and Schnörr, 2007), and methods that incorporate physical constraints within their regularization schemes (Schmidt and Sutton, 2019; Ruhnau et al, 2007; Cuzol et al, 2007; Papadakis et al, 2007; Weickert and Schnörr, 2001b).

Despite this body of work, comparatively little research has been done in terms of the UQ and error analysis of OFME methods, especially within the context of fluid velocimetry. To be sure, there are several important papers on the mathematical analysis of OFME methods in the literature (Aubert and Kornprobst, 1999; Aubert et al, 1999; Wang et al, 2015). However, these studies focus on fundamental analytical problems such as well-posedness and convergence,

as opposed to the more applied problems of UQ and error analysis.

Within the UQ and error analysis literature itself, most studies focus on the estimation of confidence in OF measurements in order to identify unreliable vectors for weighting or pruning prior to subsequent processing (Barron et al, 1994; Haußecker and Spies, 2000; Kondermann et al, 2007, 2008; Kybic and Nieuwenhuis, 2011; Gehrig and Scharwächter, 2011; Mac Aodha et al, 2012; Brumm et al, 2015; Wannenwetsch et al, 2017). While many confidence measures — from photometric proxy metrics such as the image intensity gradient (Barron et al, 1994) or the Horn-Schunck cost function (2) (Brumm et al, 2015), to statistical and probabilistic metrics (Kondermann et al, 2008; Wannenwetsch et al, 2017), to metrics computed with machine learning methods (Gehrig and Scharwächter, 2011; Mac Aodha et al, 2012) — have been developed, these measures are *post hoc* and empirical. Moreover, these measures are designed for rigid and quasi-rigid body motion estimation; they are primarily used to improve the accuracy of OF estimates by rejecting spurious vectors (Kybic and Nieuwenhuis, 2011).

In addition to these studies on confidence measures, there are a few papers on UQ and perturbation analysis of OFME. For example, Sun et al (2018) break from the convention of treating OFME deterministically and, instead, treat OFME in terms of a statistical inverse problem. The result is a Bayesian OFME framework that yields not only "point" estimates of the OF field, but also statistical estimates, such as the uncertainty of the measured field. However, this framework does not enable the prediction of uncertainty prior to the computation of the OF estimate itself. We also note that Sun et al (2018) demonstrate their framework for rigid body motion only.

Cai et al (2017) also propose a stochastic framework for 2D OF estimation in turbulent fluid flows. Unlike the method of Sun et al (2018), which is founded on a Bayesian interpretation of the OFME problem, this framework relies on a stochastic decomposition of the fluid flow into a large scale "motion" component and a small scale "uncertainty" component. The resulting framework naturally incorporates a notion of uncertainty in the OF measurement. However, as with the method of Sun et al (2018), this framework does not provide a means of *a priori* error analysis.

Liu et al (2008; 2015) also address uncertainty in OFME fluid velocimetry; the 2008 paper is mainly concerned with the relationship between the OF field and fluid velocity field, whereas the 2015 paper addresses differences between OF and PIV. Both papers present a perturbation analysis for a physics-based OFME scheme

designed for fluid motion estimation. Specifically, their analysis yields an error-propagation equation that relates the noise in the images to the error in the estimated velocity field.

In this paper, we focus on identifying and quantifying the sources of error in differential OFME methods. In particular, we propound an *a priori* error analysis of the GCE for double-frame, single-exposure problems. In addition to being the prototypical photometric constraint equation of OFME, the GCE is particularly amenable to mathematical analysis; it is linear in the unknown OF field $\underline{u}$, and the corresponding estimation problem can be cast in a standard linear least squares form. This, in turn, opens the estimation problem up to rigorous study by error analysis techniques for PDEs.

To this end, we derive an *a priori* error bound for the estimated OF flow field using these error analysis techniques. We then interpret this error bound with the goal of gaining insight into the nature and limitations of OFME methods more generally. Finally, we present numerical demonstrations of the error bound based on 3D data sets of homogeneous isotropic turbulence (HIT) and transitional boundary layer flow (BL) generated from direct numerical simulations (DNS) conducted by researchers at Johns Hopkins University (JHU) (Perlman et al, 2007; Li et al, 2008; Zaki, 2013).

We note that by limiting our analysis to the GCE, we do not treat complex physical effects that may arise in actual fluid velocimetry experiments. These include non-solenoidal convection, molecular diffusion, chemical reaction and, in the 2D case, out-of-plane motion of flow tracers. These effects may be treated by analysing more sophisticated OF constraint equations, such as those reviewed by Heitz et al (2009). By focusing on the GCE, we also limit our analysis to OFME problems characterized by small intensity displacements. In other words, we do not treat multi-resolution schemes (Enkelmann, 1988; Mémin and Pérez, 1998; Cohen and Herlin, 1999; Ruhnau et al, 2004, 2007; Heitz et al, 2008) or warping operator schemes (Brox et al, 2004; Papenberg et al, 2006; Brox and Malik, 2010), even though such methods are commonplace due to their ability to handle large intensity displacements (Heitz et al, 2009). In addition, we do not treat methods that employ explicit regularization strategies. Finally, we assume that the flow tracers perfectly track the flow, and we do not consider noisy intensity fields. By narrowing our scope to such an extent, it becomes possible to propound in detail a mathematically rigorous UQ of OFME fluid velocimetry. Our hope is that this analysis may serve as an insightful foundation for error analyses of OFME problems that are encountered in practice.

2 Problem statement

2.1 Mathematical preliminaries

2.1.1 Definitions from functional analysis

To make our analysis precise, we first define some concepts from functional analysis. Here we state these definitions in their technical forms and provide intuitive interpretations where appropriate. The interested reader can find these definitions in standard textbooks on variational and finite element analysis of PDEs (Quarteroni and Valli, 1997; Brenner and Scott, 2008; Ern and Guermond, 2010).

We begin with two useful function norms and spaces. The $L^\infty(\Omega)$ norm of a continuous function $f : \Omega \to \mathbb{R}$ is defined as

$$\|f\|_{L^\infty(\Omega)} := \max_{\underline{x} \in \Omega} |f(\underline{x})|.$$

In general, the $L^\infty(\Omega)$ norm of a matrix-valued function is defined as the maximum over the $L^\infty(\Omega)$ norms of the individual scalar components of the function. Meanwhile, the function space $L^\infty(\Omega)$ corresponding to this norm is defined as

$$L^\infty(\Omega) := \{f \ | \ \|f\|_{L^\infty(\Omega)} < \infty\}.$$

That is, $L^\infty(\Omega)$ is the space of all functions $f : \Omega \to \mathbb{R}$ that are bounded almost everywhere. Later, we also refer to the $L^\infty(\Omega \times T)$ norm and space, which are defined analogously over the space-time domain $\Omega \times T$.

The $L^2(\Omega)$ norm of a function $\underline{g} : \Omega \to \mathbb{R}^m$ is defined as

$$\|\underline{g}\|_{L^2(\Omega)} := \left(\int_\Omega \|\underline{g}\|_2^2 \mathrm{d}\underline{x} \right)^{1/2},$$

where $\| \cdot \|_2$ denotes the Euclidean norm. Meanwhile, the function space $L^2(\Omega)^m$ is defined as

$$L^2(\Omega)^m := \{\underline{g} \ | \ \|\underline{g}\|_{L^2(\Omega)} < \infty\}.$$

That is, $L^2(\Omega)^m$ is the set of all functions $\underline{g} : \Omega \to \mathbb{R}^m$ that are square-integrable. In this work, $m = 1$ or $m = n_\mathrm{d}$ depending on whether $\underline{g}$ is scalar- or vector-valued.

For convenience, we also define the qth-order n_d-dimensional (weak) derivative $D^q f$ of $f : \Omega \to \mathbb{R}$ as follows. First, we let $Df : \Omega \to \mathbb{R}^{n_\mathrm{d}}$ be the $n_\mathrm{d} \times 1$ matrix whose components are given by

$$(Df)_i := \frac{\partial f}{\partial x_i}, \quad i = 1, \dots, n_\mathrm{d}.$$

Second, we let $D^2 f : \Omega \to \mathbb{R}^{n_\mathrm{d} \times n_\mathrm{d}}$ be the $n_\mathrm{d} \times n_\mathrm{d}$ matrix whose components are given by

$$(D^2 f)_{ij} := \frac{\partial^2 f}{\partial x_i x_j}, \quad i, j = 1, \dots, n_\mathrm{d}.$$

Finally, we let $D^q f$ be the q-dimensional matrix of the qth derivatives of f.

2.1.2 Definitions of discrete operators

We conclude our discussion of mathematical preliminaries by laying out our formalism for the finite resolution of the measured intensity fields. To begin, we consider a uniform tessellation $\mathcal{T}_h := \{K_k\}_{k=1}^{N_K}$ of Ω. In 2D, $\mathcal{T}_h$ consists of N_K square *pixels* K of side length h, and in 3D, $\mathcal{T}_h$ consists of N_K cubic *voxels* K of side length h.

We now define the discrete operators that we use in our analysis. Firstly, we define the discretized integration operator $\int_{\Omega,h} \cdot \, \mathrm{d}\underline{x} : L^\infty(\Omega) \to \mathbb{R}$ as

$$\int_{\Omega,h} I(\underline{x},t)\mathrm{d}\underline{x} := \sum_{K \in \mathcal{T}_h} h^{n_\mathrm{d}} I(\underline{x}_\mathrm{c}^{(K)},t),$$

where $\underline{x}_\mathrm{c}^{(K)} \in \Omega$ is the centroid of $K \in \mathcal{T}_h$. This is precisely the midpoint rule of numerical integration.

Secondly, we define the n_d-dimensional rectangular filter $\Pi_h* : L^\infty(\Omega) \to L^\infty(\Omega)$ as

$$(\Pi_h * I)(\underline{x},t) := \int_\Omega I(\underline{y},t)\Pi_h(\underline{x} - \underline{y})\mathrm{d}\underline{y} \quad \forall \underline{x} \in \Omega,$$

where $\Pi_h : \mathbb{R}^{n_\mathrm{d}} \to \mathbb{R}$ is the n_d-dimensional rectangular function that satisfies

$$\Pi_h(\underline{x}) = \begin{cases} 1/h^{n_\mathrm{d}} & \underline{x} \in (-h/2, h/2)^{n_\mathrm{d}}, \\ 0 & \text{otherwise.} \end{cases}$$

We adopt this definition because we choose to model the *measured* intensity fields as the *true* intensity field $I : \Omega \times T \to \mathbb{R}$ spatially averaged over square or cubic regions of side length h. Specifically, we model the measured intensity field pair $I_h \in L^\infty(\Omega)^2$ according to

$$I_h := \{I_{h,\mathrm{i}} : \Omega \to \mathbb{R}, I_{h,\mathrm{f}} : \Omega \to \mathbb{R}\}$$
$$:= \{\Pi_h * I(\cdot, t_0), \Pi_h * I(\cdot, t_0 + \Delta t)\},$$

where the subscripts i and f signify the initial and final image frames, respectively.

Thirdly, we define the sliding finite difference operator $\underline{\nabla}_h : L^\infty(\Omega) \to L^\infty(\Omega)^{n_\mathrm{d}}$ according to

$$(\underline{\nabla}_h I)(\underline{x},t)_i := \frac{1}{2h}(I(\underline{x} + h\underline{e}_i, t) - I(\underline{x} - h\underline{e}_i, t))$$

$\forall \underline{x} \in \Omega$, $i = 1, \ldots, n_\mathrm{d}$. Here $\{\underline{e}_i\}_{i=1}^{n_\mathrm{d}}$ is the standard basis of an n_d-dimensional coordinate space, and t is an arbitrary instant of time in T. We note that this operator provides a central difference approximation of gradients with second-order accuracy in space.

Fourthly, we define the time-averaged sliding finite difference operator $\overline{\underline{\nabla}}_h : L^\infty(\Omega)^2 \to L^\infty(\Omega)^{n_\mathrm{d}}$ as

$$\overline{\underline{\nabla}}_h I_h := \frac{1}{2}(\underline{\nabla}_h I_{h,\mathrm{i}} + \underline{\nabla}_h I_{h,\mathrm{f}}).$$

In addition to being second-order accurate in space, this time-averaged finite difference operator is second-order accurate in time at $t^* := t_0 + \Delta t/2$. This is important because, in this paper, we limit ourselves to double-frame, single exposure problems, for which we can achieve a maximum of second-order accuracy in time.

Finally, we define the temporal finite difference operator $\partial_{t,\Delta t} I_h : L^\infty(\Omega)^2 \to L^\infty(\Omega)$ as

$$\partial_{t,\Delta t} I_h := (I_{h,\mathrm{f}} - I_{h,\mathrm{i}})/\Delta t.$$

As with the $\overline{\underline{\nabla}}_h$ operator, the $\partial_{t,\Delta t}$ operator is second-order accurate in time at the midpoint time t^*.

2.2 Motion estimation problem

We can now formalize our motion estimation problem. We assume that we are given a smooth, time-dependent intensity field I that satisfies (1). In addition, we limit our focus to OFME schemes without explicit regularization. As such, we express the solution of our OFME problem as

$$\underline{u}(\cdot, t) = \arg\min_{\underline{w}} \int_\Omega \left(\partial_t I(\underline{x},t) + \underline{\nabla} I(\underline{x},t) \cdot \underline{w}(\underline{x})\right)^2 \mathrm{d}\underline{x} \quad (3)$$

for a given time $t \in T$.

Strictly speaking, (3) is not well-posed; we need to specify the *approximation space* within which to search for the minimizer of the functional in (3). To this end, we introduce a basis $\{\underline{\phi}^{(j)} : \Omega \to \mathbb{R}^{n_\mathrm{d}}\}_{j=1}^n$ and define an arbitrary approximation $\underline{w}_n : \Omega \to \mathbb{R}^{n_\mathrm{d}}$ of $\underline{u}(\cdot, t)$ by

$$\underline{w}_n(\underline{x}) := \sum_{j=1}^n c_j \underline{\phi}^{(j)}(\underline{x}) \quad \forall \underline{x} \in \Omega, \quad (4)$$

where $c_j \in \mathbb{R}$, $j = 1, 2, \ldots, n$, are arbitrary coefficients. For a prescribed value of n, we may then define the n-dimensional approximation space $\mathcal{W}_n$ as

$$\mathcal{W}_n := \mathrm{span}\{\underline{\phi}^{(j)}\}_{j=1}^n. \quad (5)$$

Of course in practice, one needs to choose or learn a basis for $\underline{w}_n$. Possible basis functions include *radial basis functions* (Lowitzsch, 2004; Macêdo and Castro, 2008), *wavelets* (Wu et al, 2000; Schmidt and Sutton, 2019, 2020; Kadri-Harouna et al, 2013) and *Legendre polynomials*. In fact, the Lucas-Kanade (1981; 1984) method of OFME can be viewed as a special case of

the framework defined by (3) and (4) with *piecewise constant basis functions*.

With definitions (4) and (5), we may more precisely pose the motion estimation problem as

$$\underline{u}_n(\cdot, t) = \underset{\underline{w}_n \in \mathcal{W}_n}{\arg\min} \int_\Omega \left(\partial_t I(\underline{x}, t) + \underline{\nabla} I(\underline{x}, t) \cdot \underline{w}_n(\underline{x}) \right)^2 d\underline{x} \tag{6}$$

for a given time $t \in T$. Of course, in reality, we do not know I, $\partial_t I$ or $\underline{\nabla} I$. Instead, we can only measure $I_{h,\mathrm{i}}$ and $I_{h,\mathrm{f}}$ and evaluate $\partial_{t, \Delta t} I_h$, and $\overline{\underline{\nabla}}_h I_h$. As such, we approximate the continuous operators in (6) with the discrete operators defined in section 2.1.2 and obtain

$$\underline{u}_\delta = \underset{\underline{w}_\delta \in \mathcal{W}_n}{\arg\min} \int_{\Omega, h} (\partial_{t, \Delta t} I_h + \overline{\underline{\nabla}}_h I_h \cdot \underline{w}_\delta)^2 d\underline{x}, \tag{7}$$

where $u_\delta : \Omega \to \mathbb{R}^{n_\mathrm{d}}$ is the computable estimate of $u(\cdot, t^*)$. For notational convenience, we have introduced a set $\delta := \{n, h, \Delta t\}$ that collects the three hyperparameters associated with (7). We add δ as a subscript to the minimizer of (7) to indicate that the solution to this discretized minimization problem is parameterized by n, h, and Δt. We note that while n and Δt can readily be varied in practice, h cannot be adjusted once a camera sensor and desired field-of-view have been selected.

We conclude this section by noting that, given an explicit basis $\{\underline{\phi}^{(j)}\}_{j=1}^n$ for $\mathcal{W}_n$, (7) reduces to a standard linear least squares problem for the coefficients $\{c_j\}_{j=1}^n$ of the given basis functions.

3 *A priori* error analysis

The fact that (7) is reducible to a linear least squares problem is salient because the linear least squares problem is equivalent to the *Petrov-Galerkin problem* (Quarteroni and Valli, 1997). A key topic in the analysis of PDEs, the Petrov-Galerkin problem features in the theory that underpins a major class of finite element methods (Quarteroni and Valli, 1997; Brenner and Scott, 2008). The main contribution of this paper is the application of Petrov-Galerkin analysis techniques to differential OFME to derive an error bound for the estimated OF field u_δ. In this section, we present and interpret the error bound resulting from such an analysis.

3.1 Statement of *a priori* error bound

Let $\Omega \subset \mathbb{R}^{n_\mathrm{d}}$ be a Lipschitz domain,

$$\mathcal{W} := \{\underline{w} \in L^2(\Omega)^{n_\mathrm{d}} \mid \underline{\nabla} \cdot \underline{w} \in L^2(\Omega)\}$$

be the trial space, and

$$\mathcal{V} := L^2(\Omega)$$

be the test space. Given a smooth, time-dependent intensity field $I : \Omega \times T \to \mathbb{R}$, assume that the exact OF field $\underline{u}$ satisfies (1). Furthermore, let the estimated OF field $\underline{u}_\delta$ be given by (7), and the approximation space $\mathcal{W}_n$ corresponding to the trial space $\mathcal{W}$ be given by (5). Then, the error of $\underline{u}_\delta$ in the $L^2(\Omega)$ norm at time $t^* := t_0 + \Delta t/2$ is bounded by

$$\|\underline{u}(\cdot, t^*) - \underline{u}_\delta\|_{L^2(\Omega)}$$
$$\leq \left(1 + \frac{\gamma}{\alpha_\delta}\right) \inf_{\underline{w}_n \in \mathcal{W}_n} \|\underline{u}(\cdot, t^*) - \underline{w}_n\|_{L^2(\Omega)}$$
$$+ \frac{1}{\alpha_\delta} \left(A h^2 + B \Delta t^2 + O(h^4) + O(h^2 \Delta t^2) \right), \tag{8}$$

where the continuity constant γ is defined by

$$\gamma := \sup_{\underline{w}_n \in \mathcal{W}} \frac{\|\nabla I \cdot \underline{w}_n\|_{L^2(\Omega)}}{\|\underline{w}_n\|_{\mathcal{W}}},$$

the stability constant α_δ is bounded from the below according to

$$\alpha_\delta \geq \inf_{\underline{w}_n \in \mathcal{W}_n} \frac{\|\overline{\underline{\nabla}}_h I_h \cdot \underline{w}_n\|_{L^2(\Omega)}}{\|\underline{w}_n\|_{\mathcal{W}}} - O(h^2),$$

the expressions A and B are defined by

$$A := \big(c_{\mathrm{fdx}}\|D^3 I\|_{L^\infty(\Omega \times T)} + c_{\mathrm{f}}\|D^3 I(\cdot, t^*)\|_{L^\infty(\Omega)}$$
$$+ c_{\mathrm{q},1} \max_{0 \leq q \leq 3} \|D^q I(\cdot, t^*)\|_{L^\infty(\Omega)}\big)\|\underline{u}(\cdot, t^*)\|_{L^2(\Omega)}$$
$$+ c_{\mathrm{f}}\|D^3 I(\cdot, t^*)\|_{L^\infty(\Omega)}$$
$$+ c_{\mathrm{q},2} \max_{0 \leq q \leq 2} \|D^q \partial_t I(\cdot, t^*)\|_{L^\infty(\Omega)}$$

$$B := c_{\mathrm{t}}\|\partial_t^2 I\|_{L^\infty(\Omega \times T)} + c_{\mathrm{fdt}}\|\partial_t^3 I\|_{L^\infty(\Omega \times T)},$$
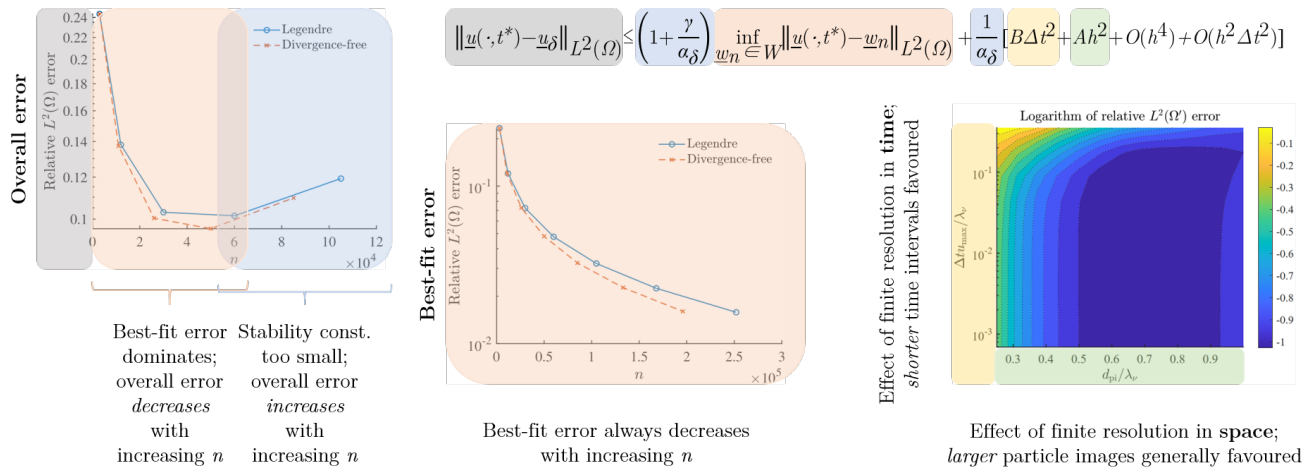
and c_{fdx}, c_{t}, c_{f}, c_{fdt}, $c_{\mathrm{q},1}$ and $c_{\mathrm{q},2}$ are coefficients that are independent of h and Δt. We prove this error bound in the appendix.

Figure 1 is a graphical summary of error bound (8). In the remainder of this section, we present a systematic interpretation of the error bound. We note that the inset graphics in figure 1 are derived from the numerical demonstrations of the error bound, the details of which we present in section 4.

3.2 Interpretation of error bound

We now make sense of the *a priori* error bound. We do so by interpreting each term in the bound individually, starting with

$$\|\underline{u}(\cdot, t^*) - \underline{u}_\delta\|_{L^2(\Omega)}.$$

$$\|\underline{u}(\cdot,t^*)-\underline{u}_\delta\|_{L^2(\Omega)} \lesssim \left(1+\frac{\gamma}{\alpha_\delta}\right)\inf_{\underline{w}_n\in W}\|\underline{u}(\cdot,t^*)-\underline{w}_n\|_{L^2(\Omega)} + \frac{1}{\alpha_\delta}[B\Delta t^2 + Ah^2 + O(h^4) + O(h^2\Delta t^2)]$$

Best-fit error always decreases with increasing n

Effect of finite resolution in **space**; *larger* particle images generally favoured

Fig. 1 Graphical overview of error bound (8). Terms and coefficients in the error bound are color-coded along with their associated graphics. The construction and meaning of these graphics is detailed in section 4. The best-fit approximation error (peach) always decreases as the dimension n of the approximation space increases. This causes the overall error (gray) to initially decrease precipitously. At the same time however, the stability constant (blue) decreases as n increases, eventually causing overall error to increase with increasing n. Meanwhile, finite-resolution effects are accounted by the leading-order terms Ah^2 (green) and $B\Delta t^2$ (yellow). In the case of particle-based velocimetry, these effects are minimized by choosing a large particle-image diameter — which results in smoother images — and, in the absence of noise, minimizing the time interval between particle-image frames.

This quantity is the $L^2(\Omega)$ error of the estimate $\underline{u}_\delta$ relative to the exact OF field $\underline{u}(\cdot,t^*)$. We call this the estimation error.

The quantity

$$\inf_{\underline{w}_n\in\mathcal{W}_n}\|\underline{u}(\cdot,t^*)-\underline{w}_n\|_{L^2(\Omega)}$$

is the *best-fit* error, which quantifies the fidelity with which we can represent the true OF field $\underline{u}(\cdot,t^*)$ in a given approximation space $\mathcal{W}_n$. This error quantifies the ability of the n basis functions that span the space to approximate $\underline{u}(\cdot,t^*)$. In other words, the best-fit error reflects the "richness" of $\mathcal{W}_n$. We can view the best-fit error as a mathematical characterization of the spatial resolution of a given OFME method.

In general, as the value of n increases, the space $\mathcal{W}_n$ becomes more "enriched", and the best-fit error decreases. In practice however, the information content of the acquired data limits the extent to which we can enrich $\mathcal{W}_n$ (e.g. by increasing n). The stability constant α_δ quantifies this limitation. Also known in the analysis of PDEs as the *inf-sup* constant, α_δ quantifies our ability to infer an estimate $\underline{u}_\delta$ in the approximation space $\mathcal{W}_n$ based on $\overline{\nabla}_h I_h$. The stability constant is a mathematical characterization of the accuracy of a given OFME method.

The stability constant should be bounded away from zero; a stability constant of zero implies that the measured intensity field pair I_h contains insufficient information to infer the coefficients associated with some or all of the basis functions. In other words, a stability

constant of zero implies that the estimation problem is ill-posed. We note that the stability constant is a non-increasing function of n. That is, it decreases as the approximation space becomes more enriched. (On the other hand, the continuity constant γ is dictated solely by the information content of the acquired data; it does not depend on the particular OFME method used and only serves to rescale the parameter-dependent stability constant.) In the context of particle-based velocimetry, we note two possible scenarios in which the stability constant becomes too small: (i) There are insufficient particles in support of one or more basis functions, or (ii) the chosen value of n is too high for the number of particles present.

With expressions Ah^2 and $B\Delta t^2$, error bound (8) also accounts for the finite resolution of the measured intensity field pair I_h. Specifically, the terms

$$c_{q,1}h^2\max_{0\le q\le 3}\|D^q I(\cdot,t^*)\|_{L^\infty(\Omega)}$$

and

$$c_{q,2}h^2\max_{0\le q\le 2}\|D^q\partial_t I(\cdot,t^*)\|_{L^\infty(\Omega)},$$

as well as the $O(h^2)$ correction term appearing in the bound for α_δ account for the *quadrature error*. This is simply the error associated with the midpoint-rule approximation (7) of the integral appearing in (6). The coefficients $c_{q,1}$ and $c_{q,2}$ are associated with this type of error. In addition, the quantity

$$c_f h^2\|D^3 I(\cdot,t^*)\|_{L^\infty(\Omega)}$$

is the error associated with the spatial filtering inherent in I_h. Furthermore, the quantity

$$c_{\mathrm{t}} \Delta t^2 \|\partial_t^2 I\|_{L^\infty(\Omega \times T)}$$

is the error associated with the time averaging of I_h over the time interval Δt between frames.

The remaining terms in expressions Ah^2 and $B\Delta t^2$ account for the finite difference approximations of the temporal and spatial derivatives in (6). We start with the temporal finite difference error term

$$c_{\mathrm{fdt}} \Delta t^2 \|\partial_t^3 I\|_{L^\infty(\Omega \times T)}.$$

Because we use a second-order finite difference scheme in time, this error scales with the third temporal derivative of I and quadratically with Δt. In the absence of noise, this error decreases as Δt decreases. We note that Liu and Shen (2008; 2015) find a commensurate relationship for a first-order temporal finite difference scheme.

This scaling reveals why differential OFME methods are regarded as being ill-suited to particle-based velocimetry experiments exhibiting large particle displacements. As Sugii et al (2000) summarize, differential OFME methods "cannot measure large displacements because of [their] small dynamic range". Indeed, this scaling has served as an impetus for the development of numerous variations of differential OFME, such as multi-resolution schemes (Enkelmann, 1988; Mémin and Pérez, 1998; Cohen and Herlin, 1999; Ruhnau et al, 2004, 2007; Heitz et al, 2008), warping schemes (Brox et al, 2004; Papenberg et al, 2006; Brox and Malik, 2010), hybrid PIV-OFME schemes (Sugii et al, 2000; Yang and Johnson, 2017), and wavelet-based schemes (Wu et al, 2000; Schmidt and Sutton, 2019, 2020).

On the other hand, the quantity

$$c_{\mathrm{fdx}} h^2 \|D^3 I\|_{L^\infty(\Omega \times T)}$$

is the spatial finite difference error. Because we use a second-order centered difference scheme in space, this error scales with the third spatial derivative of I and quadratically with h.

This scaling has interesting practical ramifications in the context of particle-based velocimetry. If we define the particle image diameter d_{pi} in terms of h (e.g. $d_{\mathrm{pi}} = Rh$ for a fixed constant $R \sim O(1)$), this error decreases as R increases. This is because $\|D^3 I\|_{L^\infty(\Omega \times T)} \propto d_{\mathrm{pi}}^{-3}$. This means that while we cannot adjust h once a camera sensor and desired field-of-view have been selected, we can still minimize the spatial finite difference error by maximizing the particle image diameter, either by optical or numerical filtering.

The remaining terms in error bound (8) are fourth order in spacetime. The interested reader can consult

Total domain Ω_{tot}	$[0, 2\pi]^3$
Grid	1024^3 nodes
Viscosity ν	0.000185
Simulation time-step	0.0002
Time interval of simulation	$[0, 10.056]$
Total kinetic energy $E_{\mathrm{tot}} = \frac{1}{2}\overline{u_i u_i}$	0.705
RMS velocity $u' = (\frac{2}{3}E_{\mathrm{tot}})^{1/2}$	0.686
Average dissipation $\bar{\varepsilon} = 2\nu\overline{s_{ij}s_{ij}}$	0.103
Taylor length scale $\lambda = (15\nu(u')^2/\bar{\varepsilon})^{1/2}$	0.113
$\mathrm{Re}_\lambda = u'\lambda/\nu$	418
Kolmogorov time scale $\tau_\eta = (\nu/\bar{\varepsilon})^{1/2}$	0.0424
Kolmogorov length scale $\eta = (\nu^3/\bar{\varepsilon})^{1/4}$	0.00280
Integral length scale	1.364

Table 1 Parameters and statistics of JHU forced isotropic DNS data (Perlman et al, 2007; Li et al, 2008). Turbulence statistics are time averaged over time interval $[0, 10.056]$.

the appendix for the exact forms of these higher order terms.

4 Numerical demonstrations of error bound

We now present numerical demonstrations of the derived error bound. All demonstrations are based on solutions of the discretized motion estimation problem (7) using piecewise continuous Legendre polynomials and divergence-free (DF) polynomials. For the sake of brevity, we do not describe the implementation of this method here; the interested reader can find these details in (Kumashiro, 2019). Instead, we focus on the results of this method as they pertain to the error analysis presented in this paper.

### 4.1 Description of reference data set

The reference data set for these demonstrations is derived from the DF forced isotropic DNS data provided by JHU (Perlman et al, 2007; Li et al, 2008). In particular, we use a single snapshot of the forced isotropic turbulence DNS solution originally computed on a large grid with 1024^3 nodes. Table 1 summarizes the parameters and statistics of this data set. In addition, figure 2 shows a 3D vector plot of the velocity solution over a 55^3-node subsection at the center of the total domain, and figure 3 shows the velocity magnitude over a slice cutting through the center of this smaller domain. In the remainder of this paper, we use Ω to denote the aforementioned subsection and Ω_{tot} to denote the total domain.

As stated in table 1, $\Omega_{\mathrm{tot}} = [0, 2\pi]^3$, and there are originally 1024^3 nodes in Ω_{tot}. As such, Ω is a cubic domain with length $(55-1)/(1024-1) \times 2\pi \approx 0.332$. Assuming that the correlation of Buch and Dahm (1996)
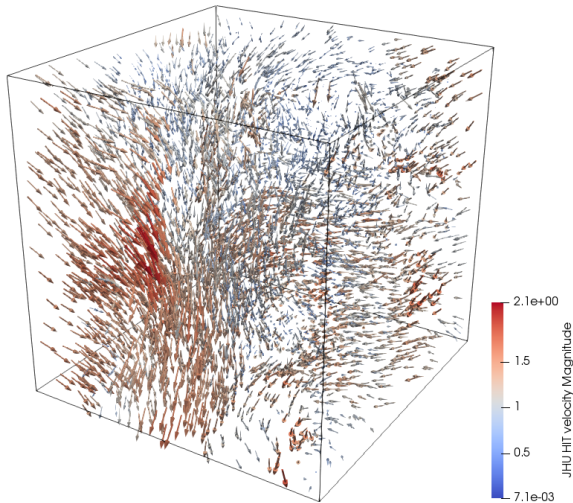
Fig. 2 Three-dimensional quiver plot of the JHU forced isotropic DNS data. This figure shows a $55 \times 55 \times 55$-node subsection Ω at center of Ω_{tot}.
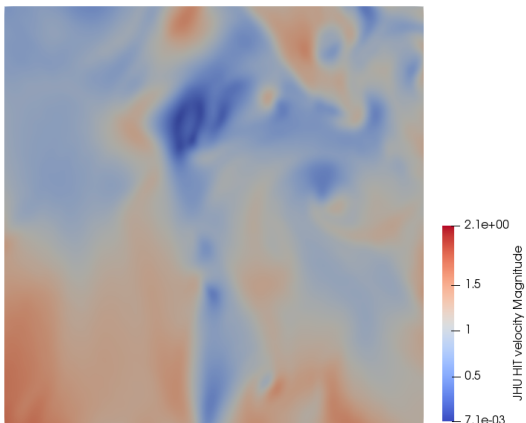
Fig. 3 Velocity magnitude of the JHU forced isotropic DNS data plotted over a central slice of the domain Ω shown in figure 2.

applies, we find that the viscous length scale for the reference velocity field is

$$\lambda_\nu \approx 6\eta = 0.0168.$$

As such, the volume of Ω is approximately $(20\lambda_\nu)^3$.

4.2 Preprocessing of reference data set

The raw DNS velocity field over Ω has 55 nodes in each direction. This corresponds to approximately three computational cells per viscous length, which is too low for an informative evaluation of the proposed method. Instead, we first supersample the DNS velocity field so that we have 16 voxels (vx) per viscous length, which

is representative of PIV experiments that attempt to capture the majority of the turbulent kinetic energy (Lavoie et al, 2007). The resulting velocity field has 301 vx in each direction. We supersample the original data set by tri-cubic spline interpolation with not-a-knot end conditions, one of the methods recommended by JHU (Perlman et al, 2007; Li et al, 2008). We henceforth refer to this supersampled velocity field as the reference velocity field $\underline{u}_{\mathrm{ref}}$.

### 4.3 Synthesis of 3D particle image intensity fields

We synthesize our 3D particle image pairs as follows. First, we seed $\underline{u}_{\mathrm{ref}}$ with a prescribed number N of point particles according to a uniform random distribution. Then, we numerically convect these point particles according to a four-stage explicit Runge-Kutta scheme coupled with piecewise tri-cubic interpolation of $\underline{u}_{\mathrm{ref}}$. In formulating the equations of motion for each particle, we assume that (i) the velocity field is static over the time between frames Δt, and (ii) the Stokes drag is negligible. Lastly, we position Gaussian intensity distributions about the positions of each point particle in both the initial and final frames. Following the recommendation of Raffel et al (2018), these particle image intensity distributions have the form

$$I_{\mathrm{pi}}(\underline{r}) = \exp\left(-8\|\underline{r}\|_2^2/d_{\mathrm{pi}}^2\right),$$

where $\underline{r}$ is the position relative to the particle image center, and d_{pi} is the particle image diameter. For ease of analysis, we assume here that d_{pi} is the same for each particle. (We later treat the case of a normally distributed d_{pi} in section 4.6.) We also assume that the particle image intensity distributions of different particles are additive, and we do not corrupt the intensity field with noise. These assumptions are intended to minimize the number of salient parameters in our demonstration. As such, they serve to simplify the interpretation of the demonstration without affecting the underlying takeaways.

4.4 Best-fit error results

Before we present the results from the estimation tests (that is, tests where $\underline{u}_{\mathrm{ref}}$ is inferred from the synthesized particle image intensity fields), we verify that the piecewise continuous Legendre and DF polynomials are capable of approximating the JHU DNS data in a best-fit error sense. For this demonstration, we divide Ω into $n_{\mathrm{IB}} = 1000$ interrogation boxes (IB), each with a volume of 31^3 vx, and solve the best-fit approximation problem using Legendre and DF polynomials that are
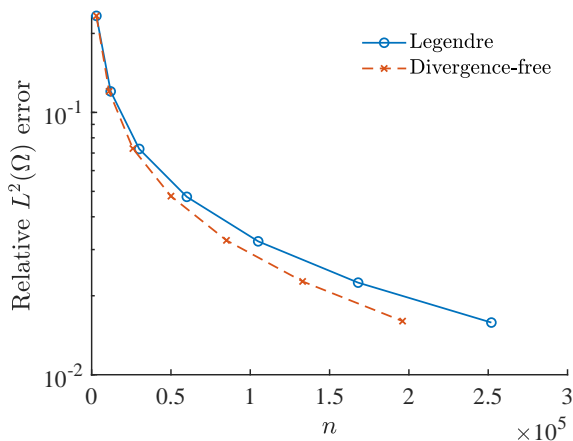
Fig. 4 Best-fit error relative to $\underline{u}_{\mathrm{ref}}$ as a function of n. The best-fit error computations are performed on the domain Ω using both Legendre and DF polynomials.

continuous within each IB. Specifically, we vary the local polynomial degree p of these piecewise continuous polynomials from zero to six and compute the best-fit error with respect to $\underline{u}_{\mathrm{ref}}$.

The results of these computations are shown in figure 4. These results are presented in terms of (i) the relative $L^2(\Omega)$ error, which is defined as

$$\|\underline{u}_{\mathrm{bf}} - \underline{u}_{\mathrm{ref}}\|_{L^2(\Omega)} / \|\underline{u}_{\mathrm{ref}}\|_{L^2(\Omega)},$$

where $\underline{u}_{\mathrm{bf}}$ is the best-fit approximation of the velocity field, and (ii) the number of basis functions n, which is related to the local polynomial degree p by

$$n = n_{\mathrm{IB}} \frac{(p+1)(p+2)(p+3)}{2} \tag{9}$$

for Legendre polynomials, and

$$n = n_{\mathrm{IB}} \left[\frac{(p+1)(p+2)(p+3)}{2} - \frac{p(p+1)(p+2)}{6} \right] \tag{10}$$

for DF polynomials. We approximate the $L^2(\Omega)$ norms by voxel-wise Riemann sums.

We make two observations based on the results in figure 4. First, we see that the best-fit error decreases with increasing n for both classes of basis functions, as expected. In terms of polynomial basis functions, we can interpret this result as follows. The complexity of a polynomial increases with its degree. As such, the higher the degree of the polynomial, the more features it is capable of resolving.

The second observation is that the best-fit error of the DF-polynomial approximation is less than or equal to that of the Legendre-polynomial approximation for a given value of n. That is, the DF polynomials provide a more "efficient" basis than the Legendre polynomials for this data set. This is simply because our data

set is divergence free (up to numerical precision), and the DF constraint affords a reduction in the number of basis functions required to span a given DF function space. As shown in (9) and (10), this dimensionality reduction is borne out transparently for polynomial basis functions. We thus note that, in addition to the *dimension* of the chosen approximation space, the *class* of approximation space can yield substantial improvements in the performance of a given OFME method.

We may gain further insights into the significance of approximation spaces by comparing our OFME scheme with PIV. Because each PIV interrogation region is assigned one independent vector, PIV intrinsically makes use of an approximation space of piecewise constant functions (i.e. zeroth degree polynomials). While this enables the application of robust cross-correlation algorithms to determine the values of these vectors (or equivalently, the coefficients of the zeroth degree polynomials), the low dimensionality of the approximation space amounts to a major limitation of PIV, particularly with respect to spatial resolution. In contrast, OFME methods can naturally accommodate complex approximation spaces and, hence, have an inherent advantage in terms of spatial resolution.

4.5 Parametric study: variation of d_{pi} and Δt

In the remainder of this section, we present and discuss results from estimation tests. The first such set of results is from a parametric study with respect to d_{pi} and Δt. For this study, we focus on a single IB Ω' located about the center of Ω. In particular, we seed $\underline{u}_{\mathrm{ref}}$ with $N = 20$ particles inside Ω' according to a uniform random distribution. This corresponds to a typical seeding density used in tomographic PIV experiments (Raffel et al, 2018; Elsinga et al, 2006; Scarano, 2012). We then convect these particles over a variable Δt and position Gaussian particle image distributions with a uniform but variable d_{pi}.

Figure 5 shows the results of this parametric study as a filled contour plot of the decimal logarithm of the relative $L^2(\Omega')$ estimation error as a function of Δt and d_{pi}. For each sampled pair of d_{pi} and Δt, we estimate $\underline{u}_{\mathrm{ref}}$ using DF polynomials of degrees zero to four and retain the estimate with the lowest relative $L^2(\Omega')$ error. For nearly all sampled pairs of d_{pi} and Δt, we find that piecewise cubic DF polynomials yield the lowest relative $L^2(\Omega')$ error. We also note that we non-dimensionalize d_{pi} as $d_{\mathrm{pi}}/\lambda_\nu$ and Δt as $\Delta t u_{\max}\lambda_\nu$, where $u_{\max}$ is the maximum velocity magnitude of $\underline{u}_{\mathrm{ref}}$ in Ω'.

The estimation error decreases with decreasing Δt. This is especially the case for small d_{pi}. In addition, the
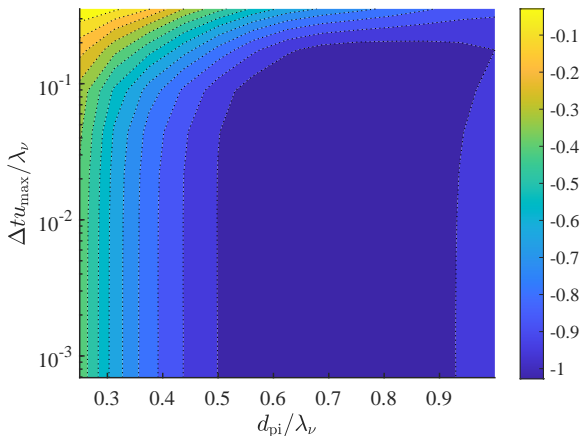
Fig. 5 The decimal logarithm of the estimation error relative to $\underline{u}_{\mathrm{ref}}$ as a function of Δt and d_{pi}. The estimation error computations are performed on a single IB Ω' located about the the center of Ω.

estimation error decreases with increasing d_{pi}. These two trends are consistent with the *a priori* error analysis, which predicts that the temporal finite difference error decreases with decreasing Δt, and the spatial finite difference error decreases with increasing d_{pi}.

However, the estimation error is not strictly monotonic with respect to d_{pi}; there is a global, albeit shallow, minimum in the estimation error. We hypothesize that this non-monotonicity is due to the error introduced in the motion constraint equation by the filtering that is inherent in the particle image intensity field. We note that we start the *a priori* error analysis with a "true" intensity field I that satisfies (1). Here the true intensity field is induced by particles and therefore does not exactly satisfy (1). This is because the particles are imaged with a finite diameter, and the motion of a given particle image is governed solely by that of its center. That is, even when the particles themselves are convected in accordance with (1), the induced intensity field is altered by a filter that introduces a residual in the motion constraint equation.

4.6 Full-scale estimation results

We now present results from estimation tests over the whole of Ω. As with the best-fit error tests, we divide Ω into $n_{\mathrm{IB}} = 1000$ IBs, each with a volume of 31^3 vx. Similar to the parametric study shown above, we seed $\underline{u}_{\mathrm{ref}}$ with 20 particles per IB. In addition, we choose a non-dimensionalized Δt of $\Delta t u_{\mathrm{max}}/\lambda_\nu = 1.25 \times 10^{-2}$ and a non-dimensionalized d_{pi} of $d_{\mathrm{pi}}/\lambda_\nu = 1$. We note that these values of Δt and d_{pi} are located inside the "valley" of the filled contour plot shown in figure 5.

(a)

(b)
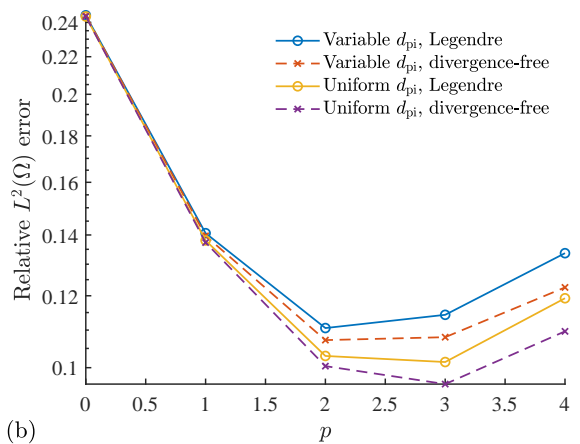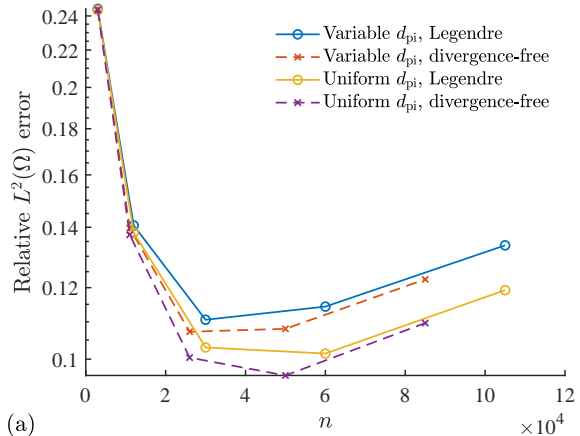
Fig. 6 Overall estimation error relative to $\underline{u}_{\mathrm{ref}}$ as a function of n and p. For the uniform d_{pi} case d_{pi} is fixed to $d_{\mathrm{pi}} = \lambda_\nu$, and for the variable d_{pi} case d_{pi} is drawn from a normal distribution with mean $d_{\mathrm{pi},\mu} = \lambda_\nu$ and standard deviation $\sigma = d_{\mathrm{pi},\mu}/3$. In both cases, $\Delta t u_{\mathrm{max}}/\lambda_\nu = 1.25 \times 10^{-2}$.

Figure 6a shows the relative $L^2(\Omega)$ error as a function of n for both Legendre and DF polynomials, while figure 6b shows the same error figures as a function of the local polynomial degree p. We see that the estimation error first decreases with increasing n (or equivalently p) but then increases once n becomes too high relative to the number of particles N. In particular, the relative $L^2(\Omega)$ error reaches a minimum when $p = 3$ for both Legendre and DF polynomials. We note that this corresponds to an n to N ratio of $n/N \approx 0.5$.

This is precisely a manifestation of the central insight of error bound (8): the competition between the best-fit error term, which decreases with increasing n, and the inverse stability constant, which increases with increasing n. That is, for $n/N < 0.5$, the effect of the best-fit error term dominates, and we attain accuracy and resolution improvements by enriching the approximation space. However, for $n/N > 0.5$, the effect of the

stability constant dominates, and the estimate worsens as we enrich the approximation space.

Of course in practice, d_{pi} is not uniform but instead varies according to some distribution. However, we can show that the effect of variable d_{pi} on the error analysis is of secondary importance to the competition between the best-fit error term and the inverse stability constant. Figures 6a and 6b show the estimation error for a corresponding set of tests where d_{pi} is drawn from a normal distribution with a mean of $d_{\mathrm{pi},\mu} = \lambda_\nu$ and a standard deviation of $\sigma = d_{\mathrm{pi},\mu}/3$. We readily see that the variable d_{pi} curves are similar to the uniform d_{pi} curves. That is, while the estimation error at a given value of n or p is higher for the variable d_{pi} case compared to the uniform d_{pi} case, the behavior of the estimation error with respect to n and p is the same regardless.

4.7 Robustness with respect to flow configuration

Finally, we show that these estimation error results are not unique to the HIT data set. To this end, we perform comparable estimation tests with the transitional BL data set provided by JHU (Zaki, 2013). Specifically, we extract from the data set a 301^3 vx subsection Ω_{BL} at the end opposite the leading edge of the BL-inducing plate; divide Ω_{BL} into $n_{\mathrm{IB}} = 1000$ IBs, each with a volume of 31^3 vx; and seed the flow with an average of 20 particles per IB. All particles are assigned the same d_{pi} as that used in the uniform d_{pi} HIT tests. The non-dimensionalized Δt is also the same as that used in the HIT tests. Figure 7 shows the velocity magnitude of the BL flow plotted over the central slice of Ω_{BL} that is normal to the free stream velocity.

Figure 8 shows the relative $L^2(\Omega_{\mathrm{BL}})$ error as a function of p for both Legendre and DF polynomials. As in figure 6b, the estimation error first decreases with increasing p but increases with increasing p once the corresponding n becomes too high relative to the number of particles N. Unlike the HIT cases however, Legendre polynomials perform better than DF polynomials, particularly for $p = 2$. This is likely because the reference velocity in this case is not DF; it contains appreciable non-solenoidal components that, by definition, cannot be resolved by DF polynomials.

5 Conclusion

We have analyzed the error of a prototypical linear OF model using error analysis techniques for PDEs. In particular, we have shown, through both rigorous mathematical analysis and numerical demonstrations, that
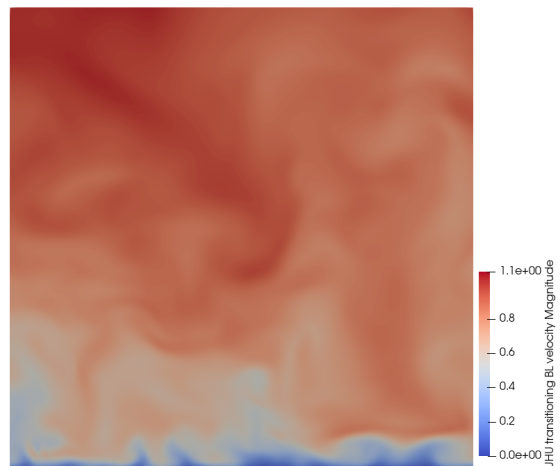
Fig. 7 Velocity magnitude of the JHU transitional BL flow plotted over a central slice of the domain Ω_{BL}. The free stream velocity is directed into the page. The BL-inducing plate lies just below the bottom of the figure.
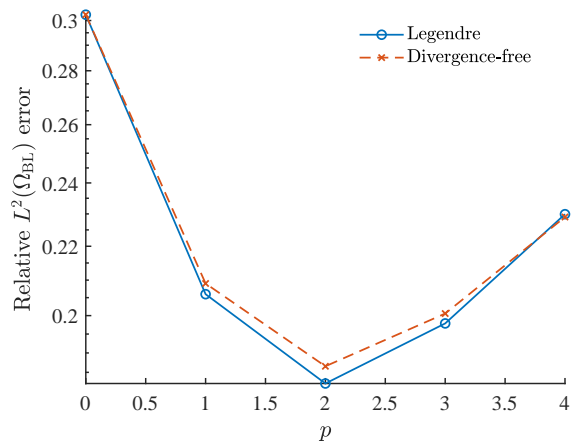
Fig. 8 Overall estimation error relative to the reference velocity inside Ω_{BF} as a function of p. The parameter values used in these tests are the same as those of the uniform d_{pi} HIT tests.

the estimation error is bounded primarily by the best-fit approximation error — which quantifies the fidelity with which one can represent the true OF field in a chosen approximation space — divided by the stability constant — which quantifies one's ability to infer the estimated OF field given the information content of the acquired data. We have also shown that the estimation error is bounded secondarily by effects related to the finite resolution, both in space and time, of the acquired data. These are the quadrature and filtering error terms — which nominally do not manifest themselves — and the finite difference and time-averaging error terms — which can significantly affect the accuracy and resolution of the estimated OF field. We reiterate that the scope of our analysis is limited to linear OFME

methods with implicit regularization (enforced through the explicit choice of approximation spaces). While this scope is admittedly narrow, it yields an OFME problem that is particularly amenable to systematic error analysis via techniques originally developed for the numerical approximation of PDEs. Our hope is that this analysis may serve as a rigorous foundation for more widely applicable error analyses of OFME methods.

A Proof of *a priori* error bound

A.1 Key lemmas

Before we prove error bound (8), we state four key lemmas required for the proof.

Lemma 1 (midpoint rule error bound) *For all twice differentiable* $f : \Omega \to \mathbb{R}$,

$$\left| \int_\Omega f \, d\underline{x} - \int_{\Omega,h} f \, d\underline{x} \right| \leq c_q h^2 \|D^2 f\|_{L^\infty(\Omega)},$$

for some c_q *independent of* h.

Proof See Theorem 8.5 of (Ern and Guermond, 2010).

Lemma 2 (filter error bound) *For any twice differentiable* $I(\cdot, t) : \Omega \to \mathbb{R}$,

$$\|I(\cdot, t) - \Pi_h * I(\cdot, t)\|_{L^\infty(\Omega)} \leq c_f h^2 \|D^2 I(\cdot, t)\|_{L^\infty(\Omega)}$$

for some c_f *independent of* h.

Proof We first introduce an n_d*-cube centered about* $\underline{x}$, $\omega(\underline{x}) := \underline{x} + (-h/2, h/2)^{n_d}$. *We then note that by the definition of the rectangular filter, for any* $\underline{x} \in \Omega$ *and* $t \in T$,

$$\left| I(\underline{x}, t) - \frac{1}{\mu(\omega(\underline{x}))} \int_{\omega(\underline{x})} I(\underline{y}, t) \, d\underline{y} \right|$$
$$= \frac{1}{\mu(\omega(\underline{x}))} \left| \int_{\omega(\underline{x})} I(\underline{y}, t) \, d\underline{y} - \mu(\omega(\underline{x})) I(\underline{x}, t) \right|$$
$$\leq \frac{1}{\mu(\omega(\underline{x}))} c_f h^2 \mu(\omega(\underline{x})) \|D^2 I(\cdot, t)\|_{L^\infty(\omega(\underline{x}))}$$
$$= c_f h^2 \|D^2 I(\cdot, t)\|_{L^\infty(\omega(\underline{x}))},$$

where $\mu(\omega(\underline{x}))$ *denotes the measure of* $\omega(\underline{x})$, *and the inequality follows from Lemma 8.4 of (Ern and Guermond, 2010).*

Lemma 3 (time-averaged finite difference error bound) *Let* $t^\star := t_0 + \Delta t/2$ *be the midpoint time in* T. *For any three-times differentiable* $I : \Omega \times T \to \mathbb{R}$,

$$\|\underline{\nabla} I(\cdot, t^*) - \overline{\underline{\nabla}}_h I\|_{L^\infty(\Omega)}$$
$$\leq c_t \Delta t^2 \|\partial_t^2 \underline{\nabla} I\|_{L^\infty(\Omega \times T)} + c_{\text{fdx}} h^2 \|D^3 I\|_{L^\infty(\Omega \times T)}$$

for some constants c_t *and* c_{fdx} *independent of* h *and* Δt.

Proof We first decompose the error as

$$\|\underline{\nabla} I(\cdot, t^\star) - \overline{\underline{\nabla}}_h I\|_{L^\infty(\Omega)}$$
$$\leq \|\underline{\nabla} I(\cdot, t^\star) - \overline{\underline{\nabla}} I\|_{L^\infty(\Omega)} + \|\overline{\underline{\nabla}} I - \overline{\underline{\nabla}}_h I\|_{L^\infty(\Omega)},$$

where $\overline{\underline{\nabla}} I := (\underline{\nabla} I(\cdot, t_0) + \underline{\nabla} I(\cdot, t_0 + \Delta t))/2$ *is the time-averaged gradient. To bound the first term, we note that the time-averaging is equivalent to evaluating the linear interpolant at the midpoint time* $t^\star$. *Hence,*

$$\|\underline{\nabla} I(\cdot, t^\star) - \overline{\underline{\nabla}} I\|_{L^\infty(\Omega)} \leq c_t \Delta t^2 \|\partial_t^2 \underline{\nabla} I\|_{L^\infty(\Omega \times T)}.$$

To bound the second term, we note that the error in the centered finite difference is bounded by

$$\|\overline{\underline{\nabla}} I - \overline{\underline{\nabla}}_h I\|_{L^\infty(\Omega)} \leq c_{\text{fdx}} h^2 \|D^3 I\|_{L^\infty(\Omega \times T)}.$$

The application of the time-averaging and finite difference bounds to the error decomposition yields the desired result.

Lemma 4 (temporal finite difference error bound) *Let* $t^\star := t_0 + \Delta t/2$ *be the midpoint time in* T. *For any* $I : \Omega \times T \to \mathbb{R}$ *that is three-times differentiable in time,*

$$\|\partial_t I(\cdot, t^*) - \partial_{t, \Delta t} I\|_{L^\infty(\Omega)} \leq c_{\text{fdt}} \Delta t^2 \|\partial_t^3 I\|_{L^\infty(\Omega \times T)},$$

for some c_{fdt} *independent of* Δt.

Proof This is a standard centered difference error bound.

A.2 Problem statement

As stated in section 2.2, the estimated OF field $\underline{u}_\delta \in \mathcal{W}_n$ is given by

$$\underline{u}_\delta = \arg\min_{\underline{w}_\delta \in \mathcal{W}_n} \int_{\Omega,h} (\partial_{t, \Delta t} I_h + \overline{\underline{\nabla}}_h I_h \cdot \underline{w}_\delta)^2 d\underline{x}.$$

We note that $\underline{u}_\delta$ is the solution to the following Petrov-Galerkin problem: Find $\underline{u}_\delta \in \mathcal{W}_n$ such that

$$a_\delta(\underline{u}_\delta, v_\delta) = \ell_\delta(v_\delta) \quad \forall v_\delta \in \mathcal{V}_\delta,$$

where $\mathcal{V}_\delta := \{v \mid v = \overline{\underline{\nabla}}_h I_h \cdot \underline{w}_n, \forall \underline{w}_n \in \mathcal{W}_n\}$ and

$$a_\delta(\underline{w}, v) := \int_{\Omega,h} v \overline{\underline{\nabla}}_h I_h \cdot \underline{w} d\underline{x} \quad \forall \underline{w} \in \mathcal{W}, \forall v \in \mathcal{V},$$
$$\ell_\delta(v) := \int_{\Omega,h} v \partial_{t, \Delta t} I_h d\underline{x} \quad \forall v \in \mathcal{V}.$$

We now assume that the true OF field $\underline{u} \in \mathcal{W} := H(\text{div}; \Omega)$ satisfies

$$a(\underline{u}, v) = \ell(v) \quad \forall v \in \mathcal{V} := L^2(\Omega),$$

where

$$a(\underline{w}, v) := \int_\Omega v \underline{\nabla} I(\underline{x}, t^*) \cdot \underline{w} d\underline{x} \quad \forall \underline{w} \in \mathcal{W}, \forall v \in \mathcal{V},$$
$$\ell(v) := \int_\Omega v \partial_t I(\underline{x}, t^*) d\underline{x} \quad \forall v \in \mathcal{V},$$

and $t^\star := t_0 + \Delta t/2$.

We wish to bound the estimation error $\|\underline{u} - \underline{u}_\delta\|_{\mathcal{W}}$.

A.3 *A priori* error estimate

To bound the estimation error, we first recall the Petrov-Galerkin error bound (e.g. Ern and Guermond, 2010):

$$
\|\underline{u} - \underline{u}_\delta\|_{\mathcal{W}} \leq \inf_{w_\delta \in \mathcal{W}_n} \Bigg[\underbrace{(1 + \frac{\gamma}{\alpha_\delta})\|\underline{u} - \underline{w}_\delta\|_{\mathcal{W}}}_{(\mathrm{I})}
$$
$$
+ \frac{1}{\alpha_\delta} \sup_{v_\delta \in \mathcal{V}_n} \underbrace{\frac{|a(\underline{w}_\delta, v_\delta) - a_\delta(\underline{w}_\delta, v_\delta)|}{\|v_\delta\|_{\mathcal{V}}}}_{(\mathrm{II})} \Bigg]
$$
$$
+ \frac{1}{\alpha_\delta} \sup_{v_\delta \in \mathcal{V}_n} \underbrace{\frac{|\ell(v_\delta) - \ell_\delta(v_\delta)|}{\|v_\delta\|_{\mathcal{V}}}}_{(\mathrm{III})}. \tag{11}
$$

We now analyze terms (I)–(III) individually.

Let us begin with (I). Here we seek a bound for the stability constant α_δ defined as (e.g. Ern and Guermond, 2010)

$$
\alpha_\delta := \inf_{\underline{w} \in \mathcal{W}_n} \sup_{v \in \mathcal{V}_n} \frac{a_\delta(\underline{w}, v)}{\|\underline{w}\|_{\mathcal{W}} \|v\|_{\mathcal{V}}},
$$

We note that the continuity constant γ is defined as (e.g. Ern and Guermond, 2010)

$$
\gamma := \sup_{\underline{w}_n \in \mathcal{W}} \frac{\|\underline{\nabla} I \cdot \underline{w}_n\|_{L^2(\Omega)}}{\|\underline{w}_n\|_{\mathcal{W}}}
$$

and, as such, is dictated by the information content of the acquired data; it does not depend on the particular OFME method used and serves only to rescale the parameter-dependent stability constant.

Before we continue with our analysis, we clarify three points regarding the notation that we use in the remainder of this proof. First, for the sake of notational convenience, we let $\hat{D}^Q f$ be the *collection* of functions $f, Df, \ldots, D^Q f$ satisfying the identity

$$
\|\hat{D}^Q f\|_{L^\infty(\Omega)} \equiv \max_{0 \leq q \leq Q} \|D^q f\|_{L^\infty(\Omega)}.
$$

Second, we introduce the simplifying notation $I^\star := I(\cdot, t^\star)$. Third, the bounding coefficients c_q and C are *generic* and, hence, reused in multiple inequalities.

We now return to our analysis. By the definition of $a_\delta(\cdot, \cdot)$ and the fact that $\|\cdot\|_{\mathcal{V}} \equiv \|\cdot\|_{L^2(\Omega)}$, α_δ specializes to

$$
\alpha_\delta = \inf_{\underline{w} \in \mathcal{W}_n} \sup_{v \in \mathcal{V}_n} \frac{\int_{\Omega, h} v \overline{\underline{\nabla}}_h I_h \cdot \underline{w} \mathrm{d}\underline{x}}{\|\underline{w}\|_{\mathcal{W}} \|v\|_{L^2(\Omega)}}.
$$

Because term (III) is *divided* by α_δ, we wish to bound α_δ from below so that $1/\alpha_\delta$ is bounded from above.

We note that the error due to the quadrature is bounded by

$$
\left| \int_\Omega v \overline{\underline{\nabla}}_h I_h \cdot \underline{w} \mathrm{d}\underline{x} - \int_{\Omega, h} v \overline{\underline{\nabla}}_h I_h \cdot \underline{w} \mathrm{d}\underline{x} \right|
$$
$$
\leq c_q h^2 \|D^2(v \overline{\underline{\nabla}}_h I_h \cdot \underline{w})\|_{L^2(\Omega)}
$$
$$
\leq C h^2 \sum_{q=0}^{2} \|D^q \overline{\underline{\nabla}}_h I_h\|_{L^\infty(\Omega)} \|D^{2-q}(\underline{w}v)\|_{L^2(\Omega)}
$$
$$
\leq C h^2 \|\hat{D}^2 \overline{\underline{\nabla}}_h I_h\|_{L^\infty(\Omega)} \|\hat{D}^2 \underline{w}\|_{L^4(\Omega)} \|\hat{D}^2 v\|_{L^4(\Omega)}
$$
$$
\leq c_{\mathrm{q},0} h^2 \|\hat{D}^2 \overline{\underline{\nabla}}_h I_h\|_{L^\infty(\Omega)} \|\underline{w}\|_{\mathcal{W}} \|v\|_{L^2(\Omega)}. \tag{12}
$$

Here the first inequality follows from the quadrature error bound (Lemma 1); the second inequality follows from Hölder's inequality; the third inequality follows from Schwarz inequality; and the last inequality follows from the equivalence of norms of functions in polynomial spaces $\mathcal{W}_n$ and $\mathcal{V}_\delta$. It hence follows that

$$
\alpha_\delta = \inf_{\underline{w} \in \mathcal{W}_n} \sup_{v \in \mathcal{V}_n} \left(\frac{\int_\Omega v \overline{\underline{\nabla}}_h I_h \cdot \underline{w} \mathrm{d}\underline{x}}{\|\underline{w}\|_{\mathcal{W}} \|v\|_{L^2(\Omega)}} \right.
$$
$$
\left. - \frac{\int_\Omega v \overline{\underline{\nabla}}_h I_h \cdot \underline{w} \mathrm{d}\underline{x} - \int_{\Omega, h} v \overline{\underline{\nabla}}_h I_h \cdot \underline{w} \mathrm{d}\underline{x}}{\|\underline{w}\|_{\mathcal{W}} \|v\|_{L^2(\Omega)}} \right)
$$
$$
\geq \inf_{\underline{w} \in \mathcal{W}_n} \sup_{v \in \mathcal{V}_n} \frac{\int_\Omega v \overline{\underline{\nabla}}_h I_h \cdot \underline{w} \mathrm{d}\underline{x}}{\|\underline{w}\|_{\mathcal{W}} \|v\|_{L^2(\Omega)}} - c_{\mathrm{q},0} h^2 \|\hat{D}^2 \overline{\underline{\nabla}}_h I_h\|_{L^\infty(\Omega)}
$$
$$
= \inf_{\underline{w} \in \mathcal{W}_n} \frac{\|\overline{\underline{\nabla}}_h I_h \cdot \underline{w}\|_{L^2(\Omega)}}{\|\underline{w}\|_{\mathcal{W}}} - c_{\mathrm{q},0} h^2 \|\hat{D}^2 \overline{\underline{\nabla}}_h I_h\|_{L^\infty(\Omega)}
$$
$$
= \inf_{\underline{w} \in \mathcal{W}_n} \frac{\|\overline{\underline{\nabla}}_h I_h \cdot \underline{w}\|_{L^2(\Omega)}}{\|\underline{w}\|_{\mathcal{W}}} - O(h^2).
$$

Here the first inequality follows from the substitution of (12) to the second term, and the second to last equality follows from choosing $v = \overline{\underline{\nabla}}_h I_h \cdot \underline{w}$.

We next analyze (II). We first decompose the term as

$$
(\mathrm{II}) = \frac{1}{\|v\|_{L^2(\Omega)}} \left(\int_\Omega v \underline{\nabla} I^\star \cdot \underline{w} \mathrm{d}\underline{x} - \int_{\Omega, h} v \overline{\underline{\nabla}}_h I_h \cdot \underline{w} \mathrm{d}\underline{x} \right)
$$
$$
= \frac{1}{\|v\|_{L^2(\Omega)}} \underbrace{\left(\int_\Omega v \underline{\nabla} I^\star \cdot \underline{w} \mathrm{d}\underline{x} - \int_{\Omega, h} v \underline{\nabla} I^\star \cdot \underline{w} \mathrm{d}\underline{x} \right)}_{(\mathrm{II.1})}
$$
$$
+ \frac{1}{\|v\|_{L^2(\Omega)}} \underbrace{\left(\int_{\Omega, h} v \underline{\nabla} I^\star \cdot \underline{w} \mathrm{d}\underline{x} - \int_{\Omega, h} v \overline{\underline{\nabla}}_h I_h \cdot \underline{w} \mathrm{d}\underline{x} \right)}_{(\mathrm{II.2})}.
$$

Term (II.1) is the error due to the quadrature and is bounded by

$$
(\mathrm{II.1}) \leq c_q h^2 \|D^2(v \underline{\nabla} I^\star \cdot \underline{w})\|_{L^2(\Omega)}
$$
$$
\leq C h^2 \sum_{q=0}^{2} \|D^{q+1} I^\star\|_{L^\infty(\Omega)} \|D^{2-q}(\underline{w}v)\|_{L^2(\Omega)}
$$
$$
\leq C h^2 \|\hat{D}^3 I^\star\|_{L^\infty(\Omega)} \|\hat{D}^2 \underline{w}\|_{L^4(\Omega)} \|\hat{D}^2 v\|_{L^4(\Omega)}
$$
$$
\leq c_{\mathrm{q},1} h^2 \|\hat{D}^3 I^\star\|_{L^\infty(\Omega)} \|\underline{w}\|_{L^2(\Omega)} \|v\|_{L^2(\Omega)}.
$$

Here the first inequality follows from the quadrature error bound (Lemma 1); the second inequality follows from Hölder's inequality; the third inequality follows from Schwarz inequality; and the last inequality follows from the equivalence of norms of functions in polynomial spaces $\mathcal{W}_n$ and $\mathcal{V}_\delta$.

To bound (II.2), we first note that

$$
\|\underline{\nabla} I^\star - \overline{\underline{\nabla}}_h I_h\|_{L^\infty(\Omega)} = \|\underline{\nabla} I^\star - \overline{\underline{\nabla}}_h(\Pi_h * I)\|_{L^\infty(\Omega)}
$$
$$
= \|\underline{\nabla} I^\star - \Pi_h * (\overline{\underline{\nabla}}_h I)\|_{L^\infty(\Omega)}
$$
$$
\leq \|\underline{\nabla} I^\star - \Pi_h * \underline{\nabla} I^\star\|_{L^\infty(\Omega)} + \|\Pi_h * (\underline{\nabla} I^\star - \overline{\underline{\nabla}}_h I)\|_{L^\infty(\Omega)}
$$
$$
\leq \|\underline{\nabla} I^\star - \Pi_h * \underline{\nabla} I^\star\|_{L^\infty(\Omega)} + \|\underline{\nabla} I^\star - \overline{\underline{\nabla}}_h I\|_{L^\infty(\Omega)}
$$
$$
\leq c_{\mathrm{f}} h^2 \|D^3 I^\star\|_{L^\infty(\Omega)} + c_t \Delta t^2 \|\partial_t^2 \underline{\nabla} I\|_{L^\infty(\Omega \times T)}
$$
$$
+ c_{\mathrm{fdx}} h^2 \|D^3 I\|_{L^\infty(\Omega \times T)} := F,
$$

where the first equality follows from the definition of the filter; the second equality follows from the commutativity of

the filter $\Pi_h *$ with the time-averaged finite difference operator $\overline{\nabla}_h$; the first inequality is the triangle inequality; the second inequality follows from the property $\|\Pi_h * f\|_{L^\infty(\Omega)} \le \|f\|_{L^\infty(\Omega)} \ \forall f$; and the last inequality follows from the filter error bound (Lemma 2) and the time-averaged finite difference error bound (Lemma 3). It follows that

$$(\text{II.2}) \le F \| \int_{\Omega,h} |v\underline{w}| \mathrm{d}\underline{x} \|_{\ell^1(\mathbb{R}^d)}$$

$$\le F(1 + c_q h^2) \|\underline{w}\|_{L^2(\Omega)} \|v\|_{L^2(\Omega)},$$

where the second inequality follows from the quadrature error bound.

Combining our results for (II.1) and (II.2), we thus find that (II) is bounded by

$$\begin{aligned}(\text{II}) \le \Big(& c_{q,1} h^2 \|\hat{D}^3 I^\star\|_{L^\infty(\Omega)} + c_f(1 + c_q h^2)h^2 \|D^3 I^\star\|_{L^\infty(\Omega)} \\ & + c_{\text{fdx}}(1 + c_q h^2)h^2 \|D^3 I\|_{L^\infty(\Omega \times T)} \\ & + c_t(1 + c_q h^2)\Delta t^2 \|\partial_t^2 I\|_{L^\infty(\Omega \times T)} \Big) \|w\|_{L^2(\Omega)} \|v\|_{L^2(\Omega)} \\ = \Big(& c_{q,1} h^2 \|\hat{D}^3 I^\star\|_{L^\infty(\Omega)} + c_f h^2 \|D^3 I^\star\|_{L^\infty(\Omega)} \\ & + c_{\text{fdx}} h^2 \|D^3 I\|_{L^\infty(\Omega \times T)} + c_t \Delta t^2 \|\partial_t^2 I\|_{L^\infty(\Omega \times T)} \\ & + O(h^4) + O(h^2 \Delta t^2) \Big) \|w\|_{L^2(\Omega)} \|v\|_{L^2(\Omega)}. \end{aligned} \tag{13}$$

This bound identifies four sources of error that are second order in h or Δt: quadrature, filtering, spatial time difference and time averaging.

Finally, we analyze (III). We first note that

$$\begin{aligned}(\text{III}) &= \frac{1}{\|v\|_{L^2(\Omega)}} \left(\int_\Omega v \partial_t I^\star \mathrm{d}\underline{x} - \int_{\Omega,h} v \partial_{t,\Delta t} I_h \mathrm{d}\underline{x} \right) \\ &= \frac{1}{\|v\|_{L^2(\Omega)}} \underbrace{\left(\int_\Omega v \partial_t I^\star \mathrm{d}\underline{x} - \int_{\Omega,h} v \partial_t I^\star \mathrm{d}\underline{x} \right)}_{(\text{III.1})} \\ & + \frac{1}{\|v\|_{L^2(\Omega)}} \underbrace{\left(\int_{\Omega,h} v \partial_t I^\star \mathrm{d}\underline{x} - \int_{\Omega,h} v \partial_{t,\Delta t} I_h \mathrm{d}\underline{x} \right)}_{(\text{III.2})}. \end{aligned}$$

Term (III.1) is the error due to the quadrature and is bounded by

$$\begin{aligned}(\text{III.1}) &\le c_q h^2 \|D^2(v \partial_t I^\star)\|_{L^2(\Omega)} \\ &\le C h^2 \sum_{q=0}^2 \|D^q \partial_t I^\star\|_{L^\infty(\Omega)} \|D^{2-q} v\|_{L^2(\Omega)} \\ &\le C h^2 \|\hat{D}^2 \partial_t I^\star\|_{L^\infty(\Omega)} \|\hat{D}^2 v\|_{L^2(\Omega)} \\ &\le c_{q,2} h^2 \|\hat{D}^2 \partial_t I^\star\|_{L^\infty(\Omega)} \|v\|_{L^2(\Omega)}. \end{aligned}$$

Here the first inequality follows from the quadrature error bound (Lemma 1); the second inequality follows from Hölder's inequality; the third inequality follows from the definition of the norms; and the last inequality follows from the equivalence of norms of functions in polynomial spaces $\mathcal{W}_n$ and $\mathcal{V}_\delta$.

To bound (III.2), we first note that

$$\begin{aligned}\|\partial_t I^\star - \partial_{t,\Delta t} I_h\|_{L^\infty(\Omega)} &= \|\partial_t I^\star - \partial_{t,\Delta t}(\Pi_h * I)\|_{L^\infty(\Omega)} \\ &= \|\partial_t I^\star - \Pi_h * (\partial_{t,\Delta t} I)\|_{L^\infty(\Omega)} \\ &\le \|\partial_t I^\star - \Pi_h * \partial_t I^\star\|_{L^\infty(\Omega)} \\ & \quad + \|\Pi_h * (\partial_t I^\star - \partial_{t,\Delta t} I)\|_{L^\infty(\Omega)} \\ &\le \|\partial_t I^\star - \Pi_h * \partial_t I^\star\|_{L^\infty(\Omega)} + \|\partial_t I^\star - \partial_{t,\Delta t} I\|_{L^\infty(\Omega)} \\ &\le c_f h^2 \|D^2 \partial_t I^\star\|_{L^\infty(\Omega)} + c_{\text{fdt}} \Delta t^2 \|\partial_t^2 I\|_{L^\infty(\Omega \times T)} =: G, \end{aligned}$$

where the first equality follows from the definition of the filter; the second equality follows from the commutativity of the filter $\Pi_h *$ with the temporal finite difference operator $\partial_{t,\Delta t}$; the first inequality is the triangle inequality; the second inequality follows from the property $\|\Pi_h * f\|_{L^\infty(\Omega)} \le \|f\|_{L^\infty(\Omega)} \ \forall f$; and the last inequality follows from the filter error bound (Lemma 2) and the temporal finite difference error bound (Lemma 4). It follows that

$$(\text{III.2}) \le G \int_{\Omega,h} |v| \mathrm{d}\underline{x} \le G(1 + c_q h^2) \|v\|_{L^2(\Omega)},$$

where the second inequality follows from the quadrature error bound.

Combining our results for (III.1) and (III.2), we thus find that (III) is bounded by,

$$\begin{aligned}(\text{III}) \le \Big(& c_{q,2} h^2 \|\hat{D}^2 \partial_t I^\star\|_{L^\infty(\Omega)} \\ & + c_f(1 + c_q h^2)h^2 \|D^2 \partial_t I^\star\|_{L^\infty(\Omega)} \\ & + c_{\text{fdt}}(1 + c_q h^2)\Delta t^2 \|\partial_t^3 I\|_{L^\infty(\Omega \times T)} \Big) \|v\|_{L^2(\Omega)} \\ = \Big(& c_{q,2} h^2 \|\hat{D}^2 \partial_t I^\star\|_{L^\infty(\Omega)} \\ & + c_f h^2 \|D^2 \partial_t I^\star\|_{L^\infty(\Omega)} \\ & + c_{\text{fdt}} \Delta t^2 \|\partial_t^3 I\|_{L^\infty(\Omega \times T)} \\ & + O(h^4) + O(h^2 \Delta t^2) \Big) \|v\|_{L^2(\Omega)} \end{aligned} \tag{14}$$

This bound identifies three sources of error that are second order in either h or Δt: quadrature, filtering and temporal time difference.

Substituting (13) and (14) into (11) and evaluating the suprema, we obtain the desired bound. $\square$

References

Álvarez L, Castano C, García M, Krissian K, Mazorra L, Salgado A, Sánchez J (2009) A new energy-based method for 3D motion estimation of incompressible piv flows. Computer Vision and Image Understanding 113(7):802–810

Aubert G, Kornprobst P (1999) A mathematical study of the relaxed optical flow problem in the space $BV(\Omega)$. SIAM Journal on Mathematical Analysis 30(6):1282–1308

Aubert G, Deriche R, Kornprobst P (1999) Computing optical flow via variational techniques. SIAM Journal on Applied Mathematics 60(1):156–182

Barron JL, Fleet DJ, Beauchemin SS (1994) Performance of optical flow techniques. International Journal of Computer Vision 12(1):43–77

Beauchemin SS, Barron JL (1995) The computation of optical flow. ACM computing surveys (CSUR) 27(3):433–466

Béréziat D, Herlin I, Younes L (2000) A generalized optical flow constraint and its physical interpretation. In: Proceedings IEEE Conference on Computer Vision and Pattern Recognition. CVPR 2000 (Cat. No. PR00662), IEEE, vol 2, pp 487–492

Bergen JR, Burt PJ, Hingorani R, Peleg S, et al (1992) A three-frame algorithm for estimating two-component image motion. IEEE Transactions on Pattern Analysis and Machine Intelligence 14(9):886–896

Brenner SC, Scott LR (2008) The mathematical theory of finite element methods. Springer New York, New York, DOI 10.1007/978-0-387-75934-0

Brox T, Malik J (2010) Large displacement optical flow: descriptor matching in variational motion estimation. IEEE transactions on pattern analysis and machine intelligence 33(3):500–513

Brox T, Bruhn A, Papenberg N, Weickert J (2004) High accuracy optical flow estimation based on a theory for warping. In: European conference on computer vision, Springer, pp 25–36

Brumm M, Marcinczak JM, Grigat RR (2015) Improved confidence measures for variational optical flow. In: VISAPP (3), pp 389–394

Buch KA, Dahm WJA (1996) Experimental study of the fine-scale structure of conserved scalar mixing in turbulent shear flows. Part 1. Sc ≫ 1. Journal of Fluid Mechanics 317:21–71

Cai S, Mémin E, Dérian P, Xu C (2017) Motion estimation under location uncertainty for turbulent fluid flows. Experiments in Fluids 59(1):8

Cohen I, Herlin I (1999) Non uniform multiresolution method for optical flow and phase portrait models: Environmental applications. International Journal of Computer Vision 33(1):29–49

Corpetti T, Mémin É, Pérez P (2002) Dense estimation of fluid flows. IEEE Transactions on pattern analysis and machine intelligence 24(3):365–380

Corpetti T, Heitz D, Arroyo G, Mémin E, Santa-Cruz A (2006) Fluid experimental flow estimation based on an optical-flow scheme. Experiments in fluids 40(1):80–97

Cuzol A, Hellier P, Mémin E (2007) A low dimensional fluid motion estimator. International Journal of Computer Vision 75(3):329–349

Elsinga GE, Scarano F, Wieneke B, van Oudheusden BW (2006) Tomographic particle image velocimetry. Experiments in Fluids 41(6):933–947

Enkelmann W (1988) Investigations of multigrid algorithms for the estimation of optical flow fields in image sequences. Computer Vision, Graphics, and Image Processing 43(2):150–177

Ern A, Guermond JL (2010) Theory and Practice of Finite Elements. Springer New York

Fleet D, Weiss Y (2005) Optical flow estimation. In: Handbook of mathematical models in computer vision, Springer, pp 237–257

Gehrig SK, Scharwächter T (2011) A real-time multi-cue framework for determining optical flow confidence. In: 2011 IEEE International Conference on Computer Vision Workshops (ICCV Workshops), IEEE, pp 1978–1985

Gibson JJ (1950) The Perception of the Visual World. Houghton Mifflin

Haußecker H, Spies H (2000) Motion. In: Computer Vision and Applications, Elsevier, pp 347–395

Haußecker HW, Fleet DJ (2001) Computing optical flow with physical models of brightness variation. IEEE Transactions on Pattern Analysis and Machine Intelligence 23(6):661–673

Héas P, Mémin E, Papadakis N, Szantai A (2007) Layered estimation of atmospheric mesoscale dynamics from satellite imagery. IEEE Transactions on Geoscience and Remote Sensing 45(12):4087–4104

Heitz D, Héas P, Mémin E, Carlier J (2008) Dynamic consistent correlation-variational approach for robust optical flow estimation. Experiments in fluids 45(4):595–608

Heitz D, Mémin E, Schnörr C (2009) Variational fluid flow measurements from image sequences: synopsis and perspectives. Experiments in Fluids 48(3):369–393

Horn BK, Schunck BG (1981) Determining optical flow. Artificial Intelligence 17(1-3):185–203

Kadri-Harouna S, Dérian P, Héas P, Mémin E (2013) Divergence-free wavelets and high order regularization. International Journal of Computer Vision 103(1):80–99

Kondermann C, Kondermann D, Jähne B, Garbe C (2007) An adaptive confidence measure for optical flows based on linear subspace projections. In: Joint Pattern Recognition Symposium, Springer, pp 132–141

Kondermann C, Mester R, Garbe C (2008) A statistical confidence measure for optical flows. In: European Conference on Computer Vision, Springer, pp 290–301

Kumashiro K (2019) A physics-constrained three-dimensional three-component particle-based velocimetry method for constant-density flows. Master's thesis, University of Toronto

Kybic J, Nieuwenhuis C (2011) Bootstrap optical flow confidence and uncertainty measure. Computer Vision and Image Understanding 115(10):1449–1462

Lavoie P, Avallone G, De Gregorio F, Romano G, Antonia R (2007) Spatial resolution of PIV for the measurement of turbulence. Experiments in Fluids 43(1):39–51

Li Y, Perlman E, Wan M, Yang Y, Meneveau C, Burns R, Chen S, Szalay A, Eyink G (2008) A public database cluster and applications to study Lagrangian evolution of velocity increments in turbulence. Journal of Turbulence 9(31)

Liu T, Shen L (2008) Fluid flow and optical flow. Journal of Fluid Mechanics 614:253–291

Liu T, Merat A, Makhmalbaf M, Fajardo C, Merati P (2015) Comparison between optical flow and cross-correlation methods for extraction of velocity fields from particle images. Experiments in Fluids 56(8):166

Lowitzsch S (2004) Approximation and interpolation employing divergence-free radial basis functions with applications. PhD thesis, Texas A&M University

Lucas BD (1984) Generalized image matching by the method of differences. PhD thesis, Carnegie-Mellon University

Lucas BD, Kanade (1981) An iterative image registration technique with an application to stereo vision. In: Proc. of the 7th Intl. Joint Conf. on Artifical Intelligence, Vancouver, British Columbia

Mac Aodha O, Humayun A, Pollefeys M, Brostow GJ (2012) Learning a confidence measure for optical flow. IEEE transactions on pattern analysis and machine intelligence 35(5):1107–1120

Macêdo I, Castro R (2008) Learning divergence-free and curl-free vector fields with matrix-valued kernels. Instituto Nacional de Matematica Pura e Aplicada, Brasil, Tech Rep

Mémin E, Pérez P (1998) Dense estimation and object-based segmentation of the optical flow with robust techniques. IEEE Transactions on Image Processing 7(5):703–719

Papadakis N, Corpetti T, Mémin E (2007) Dynamically consistent optical flow estimation. In: 2007 IEEE 11th International Conference on Computer Vision, IEEE, pp 1–7

Papenberg N, Bruhn A, Brox T, Didas S, Weickert J (2006) Highly accurate optic flow computation with theoretically justified warping. International Journal of Computer Vision 67(2):141–158

Perlman E, Burns R, Li Y, Meneveau C (2007) Data exploration of turbulence simulations using a database cluster. In: Proceedings of the 2007 ACM/IEEE Conference on Supercomputing, ACM, p 23

Quarteroni A, Valli A (1997) Numerical approximation of partial differential equations. Springer, New York, DOI 10.1007/978-3-540-85268-1

Quénot GM, Pakleza J, Kowalewski TA (1998) Particle image velocimetry with optical flow. Experiments in Fluids 25(3):177–189

Raffel M, Willert CE, Scarano F, Kähler CJ, Wereley ST, Kompenhans J (2018) Particle image velocimetry: a practical guide. Springer

Ruhnau P, Schnörr C (2007) Optical Stokes flow estimation: an imaging-based control approach. Experiments in Fluids 42(1):61–78

Ruhnau P, Kohlberger T, Schnörr C, Nobach H (2004) Variational optical flow estimation for particle image velocimetry. Experiments in Fluids 38(1):21–31

Ruhnau P, Yuan J, Schnörr C (2007) On variational methods for fluid flow estimation. In: Jähne B, Mester R, Barth E, Scharr H (eds) Complex Motion, Springer Berlin Heidelberg, Berlin, Heidelberg, pp 124–145

Scarano F (2012) Tomographic PIV: principles and practice. Measurement Science and Technology 24(1):012001

Schmidt B, Sutton J (2019) High-resolution velocimetry from tracer particle fields using a wavelet-based optical flow method. Experiments in Fluids 60(3):37

Schmidt B, Sutton J (2020) Improvements in the accuracy of wavelet-based optical flow velocimetry (wOFV) using an efficient and physically based implementation of velocity regularization. Experiments in Fluids 61(2):32

Sugii Y, Nishio S, Okuno T, Okamoto K (2000) A highly accurate iterative piv technique using a gradient method. Measurement Science and Technology 11(12):1666

Sun J, Quevedo FJ, Bollt E (2018) Bayesian optical flow with uncertainty quantification. Inverse Problems 34(10):105008

Suter D (1994) Motion estimation and vector splines. In: Proceedings of the Conference on Computer Vision and Pattern Recognition, vol 94, pp 939–942

Wang B, Cai Z, Shen L, Liu T (2015) An analysis of physics-based optical flow. Journal of Computational and Applied Mathematics 276:62–80

Wannenwetsch AS, Keuper M, Roth S (2017) Probflow: Joint optical flow and uncertainty estimation. In: Proceedings of the IEEE International Conference on Computer Vision, pp 1173–1182

Weickert J, Schnörr C (2001a) A theoretical framework for convex regularizers in PDE-based computation of image motion. International Journal of Computer Vision 45(3):245–264

Weickert J, Schnörr C (2001b) Variational optic flow computation with a spatio-temporal smoothness constraint. Journal of mathematical imaging and vision 14(3):245–255

Wu YT, Kanade T, Li CC, Cohn J (2000) Image registration using wavelet-based motion model. International Journal of Computer Vision 38(2):129–152

Yang Z, Johnson M (2017) Hybrid particle image velocimetry with the combination of cross-correlation and optical flow method. Journal of Visualization 20(3):625–638

Yuan J, Schnörr C, Mémin E (2007) Discrete orthogonal decomposition and variational fluid flow estimation. Journal of Mathematical Imaging and Vision 28(1):67–80

Zaki TA (2013) From streaks to spots and on to turbulence: exploring the dynamics of boundary layer transition. Flow, turbulence and combustion 91(3):451–473

Zhong Q, Yang H, Yin Z (2017) An optical flow algorithm based on gradient constancy assumption for PIV image processing. Measurement Science and Technology 28(5):055208